Contents lists available at ScienceDirect

Applied Catalysis B: Environmental

Oriented growth of $ZnIn_2S_4$/In(OH)$_3$ heterojunction by a facile hydrothermal transformation for efficient photocatalytic H$_2$ production

Yuexiang Li [a,*], Yali Hou [a,1], Qinyu Fu [a,1], Shaoqin Peng [a], Yun Hang Hu [b]

[a] Department of Chemistry, Nanchang University, Nanchang 330031, PR China
[b] Department of Materials Science and Engineering, Michigan Technological University, Houghton, MI 49931, USA

ARTICLE INFO

ABSTRACT

The construction of a composite photocatalyst with two suitable semiconductors is an effective strategy to improve the transport and separation of the photoexcited carrier pairs. Herein, it is the first time to report the new concept of anisotropic heterojunctions (H and J type) in layered $ZnIn_2S_4$ nanosheets as an example. Due to the anisotropic conductivity, the resistance of the electron transfer along $ZnIn_2S_4$ layers to a second semiconductor (J type heterojunction), is much less than that across the layers (H type heterojunction). As a result, the J type heterojunction can achieve higher photocatalytic activity than H type one. Furthermore, $ZnIn_2S_4$/In(OH)$_3$ heterojunction with the J type structure was successfully fabricated by a simple approach, namely, In(OH)$_3$ was selectively assembled at the rims of $ZnIn_2S_4$ nanosheets via hydrothermal transformation of the precursor precipitate with its mother solution obtained by adding Na$_2$S into the solution of stoichiometric In^{3+} and excessive Zn^{2+}. The intimate-contact J type heterojunction with in-situ photodeposited Pt shows efficient photocatalytic H$_2$ evolution under visible irradiation, leading to a high apparent quantum yield of 38.3% at 420 nm with a low optimal Pt loading of 0.25 wt%. This work provides a new insight for the development of efficient heterojunction photocatalysts with layered semiconductors.

© 2017 Elsevier B.V. All rights reserved.

1. Introduction

Hydrogen as a renewable and clean fuel has attracted extensive attention. Photocatalytic water splitting by sunlight has been considered as the most promising route for hydrogen production [1–8]. Since visible light occupies about 43% of the solar spectrum, the development of highly efficient visible-light-driven photocatalysts is of great significance. The sulfide solid solution photocatalysts, such as $(AgIn)_xZn_{2(1-x)}S_2$ [9], $Cd_{(1-x)}Zn_xS$ [10–14], and $Zn_2In_2S_4$ [15–21], have been intensively investigated due to their suitable band gaps for visible light response and tunable band structures. Besides $ZnIn_2S_4$, other $Zn_mIn_2S_{m+3}$ (m = 2–5, integer) solid solutions have also been explored as photocatalysts for hydrogen evolution [22].

The activity of a photocatalyst strongly depends on the transport and separation of the photogenerated electrons and holes. It has been well-documented that a heterojunction composite which is composed of two semiconductors with matching band edge potentials, can greatly promote the separation of the photoexcited carrier pairs to increase the photocatalytic activity [4,7]. Various heterojunctions of $ZnIn_2S_4$ have been synthesized to improve its photocatalytic performance [23–32]. For example, the tightly contacted In_2S_3/$ZnIn_2S_4$ heterojunction composite shows enhanced photocatalytic activity for H$_2$ production compared with the pure constituent component (In$_2$S$_3$ or $ZnIn_2S_4$) [23]. The 2D (dimensional) $ZnIn_2S_4$ nanosheet/1D TiO$_2$ nanorod heterojunction arrays display increased photocurrent due to the improvement of interface electron transfer [24]. ZnS-coated $ZnIn_2S_4$ shows enhanced photocatalytic hydrogen generation in the presence of glucose [25]. The introduction of carbon nanofiber into $ZnIn_2S_4$ can improve interfacial charge transfer, leading to the enhancement of photocatalytic hydrogen evolution [26]. Because RGO (reduced graphene oxide) can serve as a good electron acceptor and mediator as well as a cocatalyst, its combination with $ZnIn_2S_4$ enhances the photocatalytic efficiency for hydrogen evolution [27–31]. Layered g-C$_3$N$_4$ (graphitic carbon nitride) sheet can also promote the interfacial

---

* Corresponding author.
E-mail address: liyx@ncu.edu.cn (Y. Li).
[1] These authors contributed equally to this work.

charge transfer and thus increase the photocatalytic activity of $ZnIn_2S_4$ for hydrogen production [32].

Nevertheless, some challenges still remain for the synthesis of an efficient $ZnIn_2S_4$ composite photocatalyst. First, electrical conductivity of layered $ZnIn_2S_4$ (or $Zn_mIn_2S_{m+3}$, m = 2–5) semiconductor is anisotropic [33]. For $ZnIn_2S_4$, the ratio of the conductivity along the layers (parallel) to that across the layers (perpendicular) is about 10^3 at 300 K [33,34], namely, the resistance along the z axis is much greater than that along the x-y plane. When another semiconductor (semiconductor 2) couples onto the (0 0 1) facet of sheet-like $ZnIn_2S_4$ (H type coupling, Scheme 1), the photoinduced electron transport along z axis (across $ZnIn_2S_4$ layers) is difficult due to the high resistance, leading to low-efficient electron transfer from $ZnIn_2S_4$ to the semiconductor 2. On the other hand, when it couples at the edges of $ZnIn_2S_4$ sheets along the layered planes (J type coupling), the efficiency of electron transfer is high owing to the low resistance. Thus, compared to the H type coupling, the J type heterostructure can achieve high photocatalytic activity. However, it is difficult to selectively assemble the semiconductor 2 to $ZnIn_2S_4$ sheet rims (J type coupling). Second, $ZnIn_2S_4/Zn_mIn_2S_{m+3}$ and their composites are usually prepared by using excess of expensive organic sulfur sources such as thioacetamide (TAA) [16,17,19–25,27–32], thiourea [18] and L-cysteine [26]. Hence, it is desirable to prepare $ZnIn_2S_4/Zn_mIn_2S_{m+3}$ heterojunctions using inexpensive Na_2S.

$In(OH)_3$ is an excellent photocatalyst for the removal of aromatic compounds and reduction of CO_2 under UV irradiation [35–39]. In this work, $In(OH)_3$ was chosen as the second semiconductor to construct anisotropic $ZnIn_2S_4/In(OH)_3$ heterojunctions based on the following two reasons. 1) The potentials of conduction band (CB) edges for $ZnIn_2S_4$ (−1.1 V vs NHE, [40]) and $In(OH)_3$ (−0.93 V vs NHE, [39]) are matched, and thus the photoexcited electron can transfer from the CB of $ZnIn_2S_4$ to that of $In(OH)_3$. 2) Because $In(OH)_3$ itself cannot absorb visible light (E_g = 5.17 eV) and its potential of valence band edge (4.2 V vs NHE) is much greater than that of $ZnIn_2S_4$ (1.4 V vs NHE), $In(OH)_3$ only acts as the acceptor of the electrons photogenerated from $ZnIn_2S_4$. As a result, the carrier separation efficiency of the heterojunction depends on the electron transfer directions from $ZnIn_2S_4$ to $In(OH)_3$, namely, across or along $ZnIn_2S_4$ layers as shown in Scheme 1.

Although many heterojunctions containing $ZnIn_2S_4$ have been synthesized to improve the photocatalytic performance for hydrogen evolution and pollutant degradation [23–32], the design concept of J type heterojunction based on the anisotropic conductivity of $ZnIn_2S_4$ and the oriented growth of the J type one have not been reported. Herein, to the best of our knowledge, it is the first time to create anisotropic heterojunctions in layered $ZnIn_2S_4$ sheets, that is, $ZnIn_2S_4/In(OH)_3$ heterojunction with the J type structure has been successfully fabricated by a simple hydrothermal transformation of the precursor precipitate with its mother solution obtained by adding Na_2S into the solution of stoichiometric In^{3+} and excessive Zn^{2+}. The J type heterojunction can effectively improve the transport and separation of photoinduced carriers, leading to efficient photocatalytic H_2 evolution under visible light irradiation. This provides a general strategy to enhance photocatalytic performance for layered semiconductors such as metal oxides, RGO, MoS_2 and g-C_3N_4, which are promising photocatalyst materials for water-splitting hydrogen production [41–43].

2. Experimental

2.1. Synthesis of photocatalysts

All chemicals with analytic grade were used without further purification. $ZnIn_2S_4/In(OH)_3$ or $Zn_mIn_2S_{3+m}/In(OH)_3$ het-

erojunction was prepared by hydrothermal treatment of the co-precipitation precursor with its mother solution obtained via adding Na_2S into a mixed solution of Zn^{2+} and In^{3+}. According to stoichiometry of $ZnIn_2S_4$, except the contrast sample (1.00 mmol of $ZnSO_4·7H_2O$), the introduced amount of Zn^{2+} was excessive, whereas those of In^{3+} and $S^{2−}$ were stoichiometric. In a typical synthesis process, 1.0 mmol of $In_2(SO_4)_3·6H_2O$ and different amount of $ZnSO_4·7H_2O$ (1.00, 1.08, 1.20, 1.40 and 1.60 mmol, respectively) were dissolved in 40 mL of distilled water to obtain a mixed solution. 20 mL of the solution containing 4.0 mmol Na_2S was quickly introduced into the above mixed solution under stirring. The produced precipitate (the precursor to prepare photocatalyst) and its mother solution were transferred together into a Teflon liner with 100 mL of capacity. The liner was sealed in a stainless steel autoclave, heated at 160 °C for 12 h and then slowly cooled down to room temperature. The formed yellow powder (photocatalyst) was separated from its mother solution by centrifugation. After washing with distilled water and drying in vacuum at 80 °C for 8 h, the photocatalyst ZIS-x was obtained, where x represents the added amount of $ZnSO_4·7H_2O$ (mmol).

For comparison, pure $ZnIn_2S_4$ was synthesized by the similar hydrothermal method using TAA as the sulfur source. $In_2(SO_4)_3·6H_2O$ (1.0 mmol), $ZnSO_4·7H_2O$ (1.00 mmol) and excessive TAA (8.0 mmol) were dissolved in 60 mL of distilled water. The mixture was heated at 160 °C for 12 h. After the same separation, washing and drying procedure as above, the product was obtained and named as ZIS-TAA.

2.2. Characterization

X-ray diffraction (XRD) patterns of the samples were obtained on a XD-2/3 polycrystalline diffractometer with nickel-filtered Cu K_α radiation as the X-ray source. UV–vis absorption spectra of the samples were recorded on a Hitachi U-3310 spectrophotometer equipped with an integrating sphere by using $BaSO_4$ as the reference. The scan electron microscopy (SEM) images were taken on a JEOL JSM-6701F equipped with an energy dispersive spectrometer (EDS), and the transmission electron microscopy (TEM) and high-resolution TEM (HRTEM) images on a JEOL JEM-2100 and a JEM-2100F. The concentrations of Zn^{2+} and In^{3+} in the mother solutions of the precursors and ZIS-x samples were determined on an OPTIMA 5300DV spectrometer by inductively coupled plasma-atomic emission spectroscopy.

2.3. Photocatalytic reaction

The photocatalytic reaction was conducted in a closed Pyrex cell (235 mL, side irradiation) at room temperature. 0.10 g of a photocatalyst and 100 mL of the aqueous solution which contained 0.59 mol/L triethanolamine (TEOA), and 2.54×10^{-5} mol/L H_2PtCl_6 (the calculated Pt amount was 0.50 wt%) were added into the cell. Before the reaction, the mixture was treated in an ultrasonic bath for 5 min and bubbled with N_2 for 30 min to remove oxygen. The light source was a 350 W Xe lamp equipped with a cut-off glass filter to remove the light of wavelength below 420 nm. The total incident light intensity (420–700 nm) was determined to be 68 mW cm^{-2}. The top of the cell was sealed with a silicone rubber septum. Sampling was made intermittently through the septum. During the irradiation, the photocatalyst was remained in suspension by magnetic stirring, and metal Pt was in-situ photodeposited on the photocatalyst. The amount of photocatalytic hydrogen evolution was measured on a gas chromatography (TCD detector, 13X molecular sieve column, N_2 gas carrier). In the stability test for ZIS-1.2, the reaction system was flushed with N_2 for 30 min each 5 h irradiation.
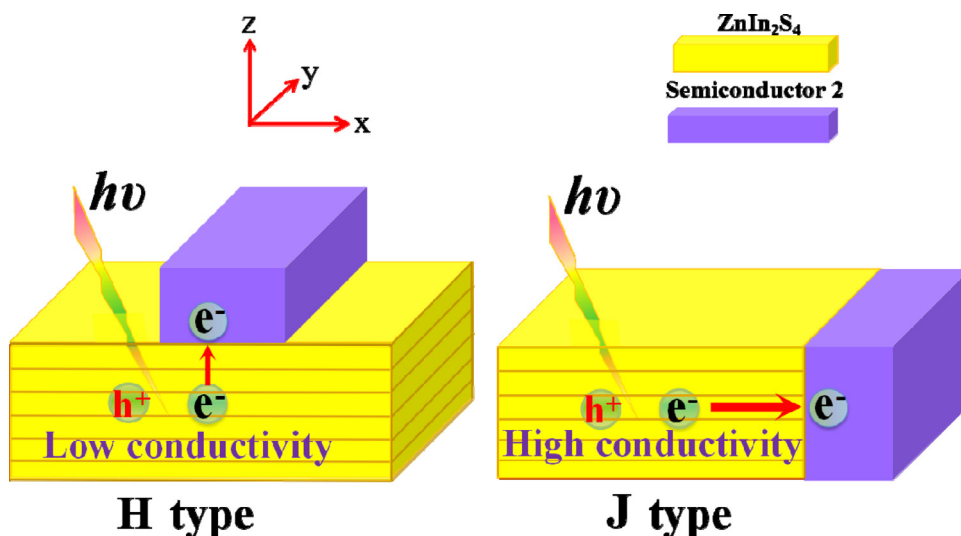
Scheme 1. Schematic of two anisotropic heterojunctions with different efficiencies of photoinduced electron transfer from layered $ZnIn_2S_4$ [along the z axis (H type) or x-y planes (J type)] to another semiconductor.

The apparent quantum yield (AQY) at 420 nm monochromatic light was estimated by the following equation.

$$AQY[\%] = 2 \times \frac{mole\ of\ hydrogen\ evolved}{mole\ of\ incident\ photon} \times 100 \qquad (1)$$

The reaction conditions including the reactor were the same as those for the above photocatalytic reaction except using a 420 nm LED lamp (UVEC-4, Shenzhen LAMPLIC Science Co Ltd, China) with the light intensity of 2.6 mw cm^{-2}.

3. Results

3.1. Properties of ZIS-x composites

The phases of various ZIS-x composites (after the hydrothermal treatment) were determined by XRD. ZIS-1.0 prepared with stoichiometric Zn^{2+} ions is a mixture of $ZnIn_2S_4$, $In(OH)_xS_y$ and ZnS (Figs. S1–3, supplementary data). All hexagonal $Zn_mIn_2S_{3+m}$ (m = 1–5) phases display similar XRD patterns [22]. The reason is that they comprise m layers of $-SZnS-$ and a repeating layer of $-SIn(o)SIn(t)S\square S-$, where (o), (t) and ($\square$) represent indium in octahedral, tetrahedral and vacant cation sites, respectively [22,34]. As shown in Fig. 1A, for ZIS-1.08 and ZIS-1.2, the strong diffraction peaks appeared at about 27.7° and 47.2° can be assigned to hexagonal $ZnIn_2S_4$ (PDF# 65-2023). However, the peak at 27.7° widens significantly for ZIS-1.4 and ZIS-1.6, which is consistent with the previous report [22]. This happens because the peak of $ZnIn_2S_4$ at 27.7° becomes weak, whereas a new strong peak at about 28.4° occurs, which can be assigned to (0 1 5) plane of hexagonal $Zn_2In_2S_5$ (PDF# 65-2129). This indicates that ZIS-1.08 and ZIS-1.2 consist of hexagonal $ZnIn_2S_4$, whereas ZIS-1.4 and ZIS-1.6 comprise both hexagonal $ZnIn_2S_4$ and $Zn_2In_2S_5$. Interestingly, the peaks of cubic $In(OH)_3$ (PDF# 76-1464) can be also observed for the ZIS-x samples (x = 1.2, 1.4 and 1.6) except ZIS-1.08, and their intensity increases greatly with increasing the x value. This demonstrates that the excessive Zn^{2+} ions improve the growth of $In(OH)_3$. Furthermore, the strong and sharp diffraction peaks indicate that the $In(OH)_3$ in the ZIS-x samples is well crystallized.

Fig. 1B shows the concentrations of Zn^{2+} and In^{3+} in the mother solutions of the precursors and photocatalysts (ZIS-1.2 and ZIS-1.6) before and after the hydrothermal treatment. Before the treatment, the concentrations of Zn^{2+} ions in the mother solutions of the two precursors are higher. However, after the treatment,
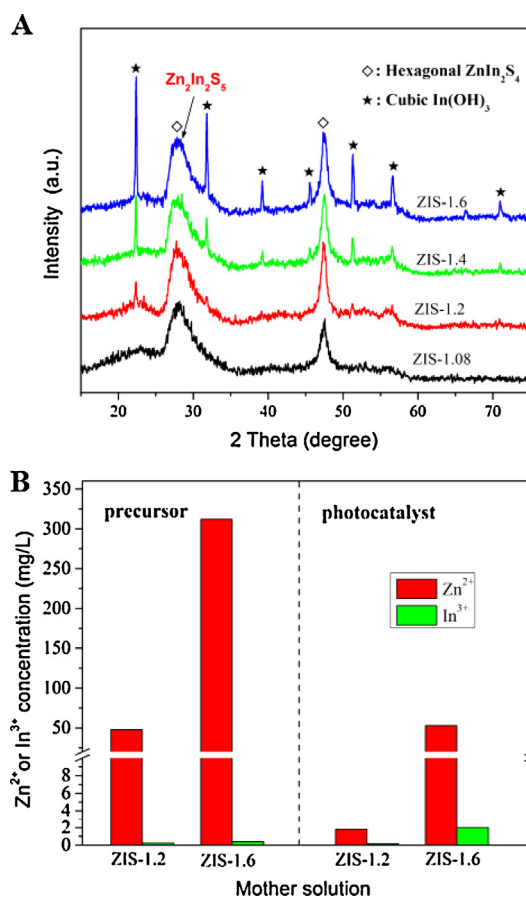

Fig. 1. A) XRD patterns of ZIS-x samples, and B) Concentrations of Zn^{2+} and In^{3+} in the mother solutions of precursors and photocatalysts before and after the hydrothermal treatment.

the concentrations in the mother solutions of the photocatalysts decrease significantly, indicating that excessive Zn^{2+} ions in the precursor mother solutions involve in the formation of their photocatalysts during the hydrothermal treatment. The difference of Zn^{2+} concentration between the mother solution of ZIS-1.6 and that of its precursor is much greater than that between ZIS-1.2 and its
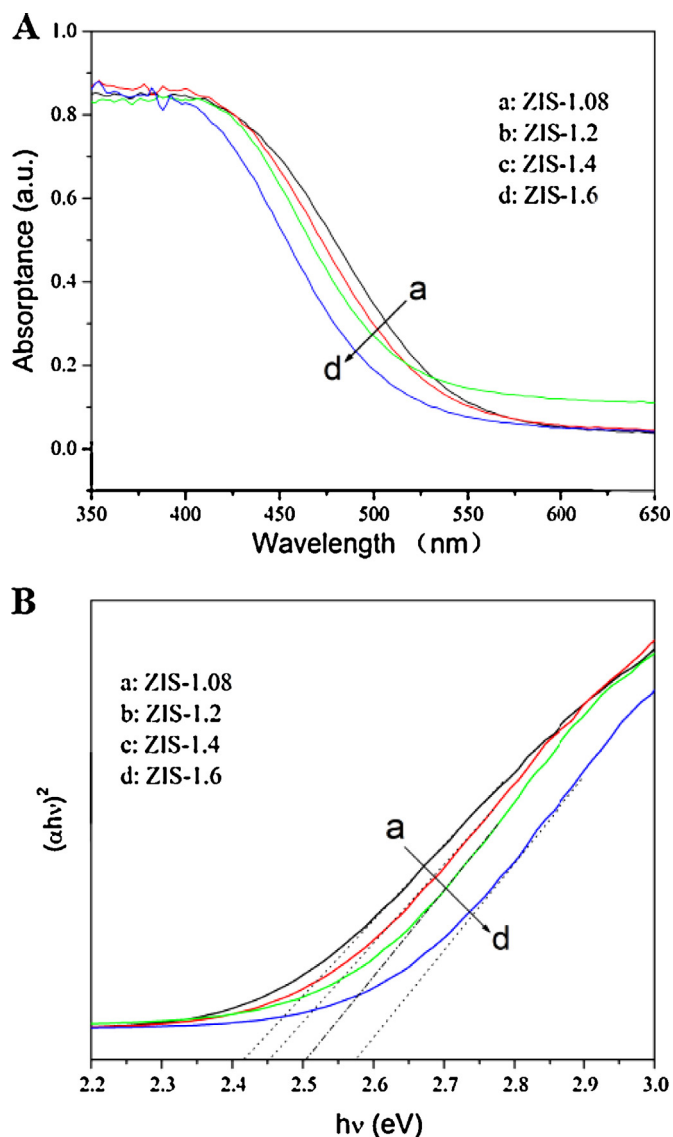
Fig. 2. A) UV–vis diffuse reflectance absorption spectra of ZIS-x samples, and B) Plots of $(\alpha h \nu)^2$ against photon energy ($h \nu$).

precursor, which supports the presence of considerable $Zn_2In_2S_5$ in ZIS-1.6 sample as shown in Fig. 1A.

The relationship between the optical properties and added amount of Zn^{2+} for ZIS-x composites was evaluated by UV–vis diffuse reflectance absorption spectroscopy. As shown in Fig. 2A, all of the composites can absorb visible light and have steep absorption edges, indicating that their absorptions are relevant to the intrinsic band gap transitions rather than the transitions from impurity levels. The absorption edges exhibit monotonic blue shift with increasing added-Zn^{2+} amount. This could be mainly attributed to the increase of $Zn_2In_2S_5$ content (Fig. 1). The band gap energy (E_g) of the samples can be obtained from plots of $(\alpha h \nu)^2$ versus photon energy $h \nu$ [18]. The E_g values of ZIS-1.08, ZIS-1.2, ZIS-1.4 and ZIS-1.6 are estimated to be 2.42, 2.45, 2.51 and 2.58 eV, respectively (Fig. 2B). The E_g values of ZIS-1.08 and ZIS-1.2 are close to that of $ZnIn_2S_4$ ($E_g = 2.46$ eV) [22], the value of ZIS-1.6 to that of $Zn_2In_2S_5$ ($E_g = 2.62$ eV) [22] and the value of ZIS-1.4 is in between, which is consistent with the XRD results (Fig. 1A).

The morphologies of the as-synthesized samples were characterized via SEM. ZIS-1.0 is composed of agglomerated grains with various sizes (Fig. S4a and b). ZIS-1.2 and ZIS-1.6 possess nanosheet

structures (Fig. 3). Furthermore, the most nanosheet edges (Fig. 3b and d) are "light" which could be indexed to $In(OH)_3$ because the conductivity of $In(OH)_3$ (Eg = 5.17 eV) is much lower than that of $ZnIn_2S_4$. This indicates the formation of J type heterojunction. A small amount of complete "light" nanosheets can also be observed for the two samples, and they are less in ZIS-1.2 than in ZIS-1.6 (Fig. 3a and c). This could be attributed to the complete covering of $Zn_mIn_2S_{m+3}$ sheets with $In(OH)_3$, namely, H type coupling. The results suggest that excessive Zn^{2+} ions promote assembly of $In(OH)_3$ at the $Zn_mIn_2S_{3+m}$ nanosheet edges (ZIS-1.2 and ZIS-1.6). However, when the Zn^{2+} concentration is too high (ZIS-1.6), the assembling selectivity for the J type heterojunction decreases significantly.

To confirm the presence of $In(OH)_3$ at the rims of $ZnIn_2S_4$ nanosheets (the oriented heterojunction), ZIS-1.2 was characterized by TEM and HRTEM. The TEM image shows that ZIS-1.2 is composed of nanosheets (Fig. 4a). The HRTEM one displays the interplanar spacing of 0.32 nm for the nanosheet bulk (Fig. 4b), indicating that its exposure facet is (0 0 1) one [44]. The spacing of the intimately-contacted edge part (width of ca. 7–11 nm) is 0.28 nm (Fig. 4b), which corresponds to that of (2 2 0) plane of cubic $In(OH)_3$. This indicates the edge part of the nanosheet is $In(OH)_3$. Those confirm that $In(OH)_3$ is selectively grown onto $ZnIn_2S_4$ nanosheets along the layered planes (horizontal direction), leading to perfectly intimate contact $ZnIn_2S_4/In(OH)_3$ junction (J type coupling), which is described by the schematic inset in Fig. 4b. The J type $ZnIn_2S_4/In(OH)_3$ heterojunction is beneficial to charge transport and separation.

3.2. Photocatalytic performance

Fig. 5A shows the effect of added-Zn^{2+} amount in the preparation process of ZIS-x composites on their photocatalytic hydrogen evolution. ZIS-1.0 exhibits the lowest photocatalytic activity (41.2 μmol) among all the samples. As the x value of ZIS-x increases, the photocatalytic activity increases to a maximum (147 μmol) at x = 1.2 and then decreases. The highest activity of ZIS-1.2 can be attributed to the formation of J type $ZnIn_2S_4/In(OH)_3$ heterojunction. The activity of ZIS-1.6 (81.0 μmol) is significantly lower than that of ZIS-1.2, probably due to following two factors: (1) The visible light absorption of ZIS-1.6 is less than that of ZIS-1.2 (Fig. 3A) because the former contains considerable $Zn_2In_2S_5$ (Fig. 1A); (2) There are more $Zn_mIn_2S_{m+3}$ (m = 1, 2, the same below) nanosheets covered with $In(OH)_3$ in ZIS-1.6 than in ZIS-1.2, namely, more H type heterojunctions (Fig. 3a and c) in ZIS-1.6. It is noteworthy that the activity of ZIS-1.2 is 4.87 times as high as that of ZIS-TAA (30.2 μmol). The apparent quantum yield (AQY) for the former reaches 38.3% at 420 nm.

H type $ZnIn_2S_4/In(OH)_3$ heterojunctions were prepared by precipitating In^{3+} in the form of $In(OH)_3$ on ZIS-TAA using sodium hydroxide (method 1, supplementary data) and ammonia solution (method 2), respectively. The molar ratio of the added In^{3+} to the $ZnIn_2S_4$ is 0.05. Compared to ZIS-TAA ($ZnIn_2S_4$), the H type $ZnIn_2S_4/In(OH)_3$ heterojunctions prepared by the two methods hardly exhibit enhanced activity for hydrogen evolution (Fig. S5, supplementary data). This can mainly be attributed to that the charge transport and separation of H type heterojunction is very low-efficient due to high resistance as shown in Scheme 1.

The photostability of ZIS-1.2 was investigated in five consecutive runs without replacing the sacrificial reagent (TEOA) solution. As shown in Fig. 6A, no obvious activity drop is observed after each run, indicating the good stability of ZIS-1.2. The activity in run 1 is lower than that in run 2, which can be attributed to the fact that the cocatalyst Pt was in situ loaded on ZIS-1.2 by photoreduction of H_2PtCl_6 in run 1. The slight decrease of the activity after run 2 is due to the decrease of TEOA concentration during the photocatalytic
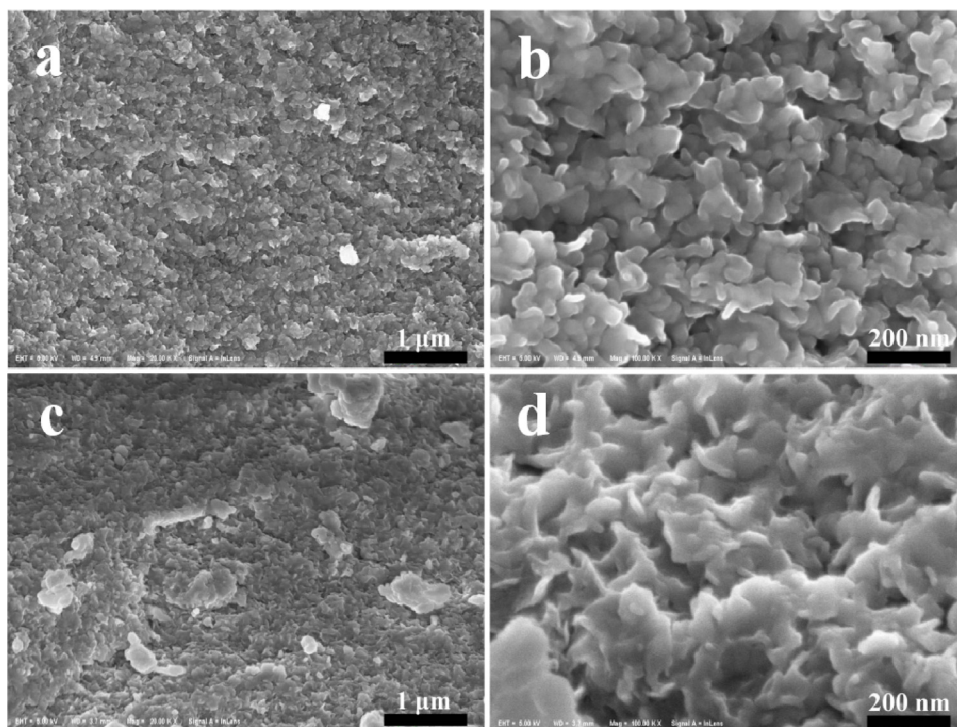
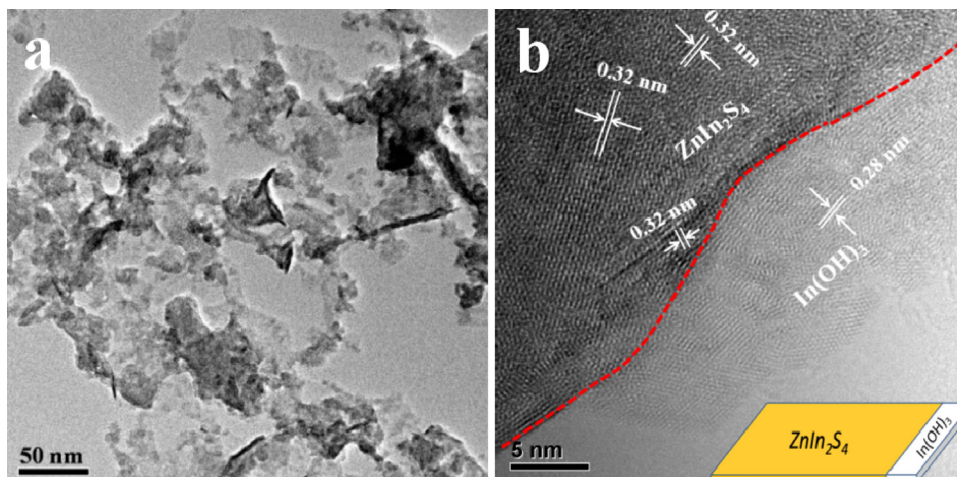**Fig. 3.** SEM images of ZIS-1.2 (a and b) and ZIS-1.6 (c and d).

Fig. 4. TEM (a) and HRTEM (b) images of ZIS-1.2.

reaction. Fig. 6B shows the effect of Pt-loading amount on the photocatalytic H_2 production over ZIS-1.2. The hydrogen production increases rapidly with increase of Pt-loading up to 0.25 wt%, then remains almost unchanged up to 0.50 wt%, and finally decreases slightly. Thus, the optimum Pt-loading is 0.25 wt%, lower than the reported values of 1.0 and 3.0 wt% for $ZnIn_2S_4$ [16,18].

4. Discussion

When a Na_2S solution was injected into the mixed solution of excessive Zn^{2+} and stoichiometric In^{3+} ions, $ZnIn_2S_4$ and $Zn_mIn_2S_{3+m}$ precipitate could form as one part of the precursor to prepare photocatalyst:

$$Zn^{2+} + 2In^{3+} + 4S^{2-} = ZnIn_2S_4 \tag{2}$$

$$mZn^{2+} + 2In^{3+} + (3+m)S^{2-} = Zn_mIn_2S_{3+m} \tag{3}$$
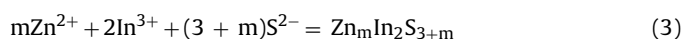
Highly excessive Zn^{2+} ions should improve the formation of $Zn_mIn_2S_{3+m}$ (m = 2) in the precursor. Due to the fast injection of the Na_2S solution, the size of the formed $Zn_mIn_2S_{3+m}$ (m = 1, 2) particles (nanosheets) should be very small.

On the other hand, In^{3+} ions in the above-mentioned mixed solutions could partly hydrolyze into mononuclear ions $In(OH)^{2+}$, $In(OH)_2^+$, and polynuclear ions $In[In(OH)_2]_n^{(3+n)+}$ [45,46], which is confirmed by the fact that the mixed solutions are acidic (Table S1, supplementary data). It has been reported that even under acidic condition, $In(OH)_xS_y$ can form [47]. As a result, when a Na_2S solution was added into the mixed solutions, the hydrolyzed In^{3+} ions would transform into $In(OH)_xS_y$ as another part of the precursor. EDS analyses demonstrate that the precursors of ZIS-1.2 and ZIS-1.6 contain considerable oxygen besides Zn, In and S (Fig. S 6A and B), confirming the formation of $In(OH)_xS_y$ in their precursors. Thus,
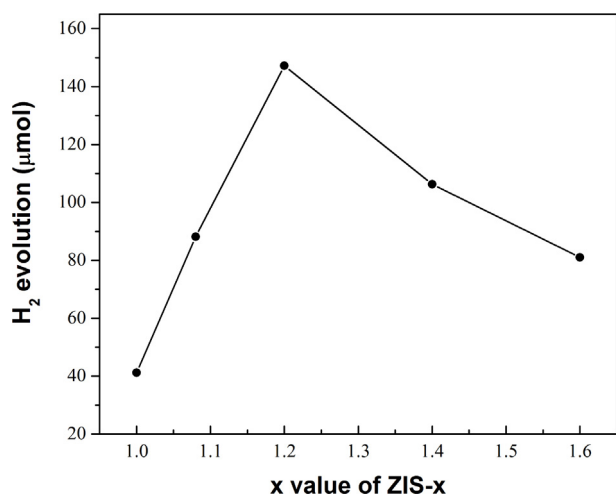
Fig. 5. Effect of added-Zn^{2+} amount in the preparation process of ZIS-x on their activity for photocatalytic H_2 evolution under visible light ($\lambda \geq 420$ nm) irradiation. Conditions: 0.10 g of ZIS-x; 100 mL of the solution containing 0.59 mol/L TEOA and 2.54×10^{-5} mol/L H_2PtCl_6 (Pt loading amount: 0.50 wt%); 350 W Xe lamp, 1 h irradiation.

the precursors of ZIS-1.2 and ZIS-1.6 are a mixture of $Zn_mIn_2S_{3+m}$ and $In(OH)_xS_y$.

During the hydrothermal treatment with elevating temperature, the smaller $Zn_mIn_2S_{3+m}$ nanosheets can dissolve and grow into the larger ones by Ostwald ripening (OR) mechanism. At the same time, the intermediate $In(OH)_xS_y$ can also solve via the following reaction:

$$In(OH)_xS_y = In^{3+} + xOH^- + yS^{2-} \qquad (4)$$
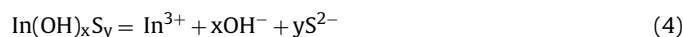
where $(x+2y)=3$. The produced S^{2-} and partial In^{3+} ions reacted with excessive Zn^{2+} to grow into $Zn_mIn_2S_{3+m}$ (m = 1 or 2) by the reactions 2 and 3, that is, the intermediate $In(OH)_xS_y$ transformed into stable $Zn_mIn_2S_{3+m}$. This led to the appearance of spare In^{3+} ions in the solution. Since the content of formed $Zn_2In_2S_5$ increased with increasing Zn^{2+} concentration in the mother solutions (Fig. 1), the In^{3+} ion content should increase with increasing Zn^{2+} concentration.

Under the hydrothermal condition (160 °C), the formed In^{3+} ions can efficiently hydrolyze into $In(OH)_3$.

$$In^{3+} + 3H_2O = In(OH)_3 + 3H^+ \qquad (5)$$

After the hydrothermal treatment, the pH values of the mother solutions of the photocatalysts decreased significantly compared to those of the precursors before the hydrothermal treatment (Table S1, supplementary data), confirming that the reactions 3 and 5 took place during the hydrothermal process.

Solubility of $In(OH)_3$ (the solubility product constant $K_{sp} = 1.3 \times 10^{-37}$) should be much higher than that for $Zn_mIn_2S_{3+m}$ because $Zn_mIn_2S_{3+m}$ is more stable than In_2S_3 ($K_{sp} = 5.7 \times 10^{-74}$). Thus, at the initial reaction stage during the hydrothermal process, only $Zn_mIn_2S_{3+m}$ grew up, whereas the formation of $In(OH)_3$ crystal nuclei would be difficult due to its high solubility. However, the produced $Zn_mIn_2S_{3+m}$ could act as crystal nuclei to improve growth of $In(OH)_3$. Because $Zn_mIn_2S_{3+m}$ possesses a nanosheet structure with stable (001) exposure facet (Fig. 4b) [44], the (100) and (010) facets perpendicular to x-y plane should be more active (high energy facets) than (001) facet. As a result, at the reaction later stage (higher In^{3+} concentration), $In(OH)_3$ could selectively grow at the edges of $Zn_mIn_2S_{3+m}$ nanosheets along the horizontal direction, namely, the formation of J type $Zn_mIn_2S_{3+m}/In(OH)_3$ heterojunctions. The formation mechanism is depicted as Scheme 2a. With increasing In^{3+} concentration during the hydrothermal pro-
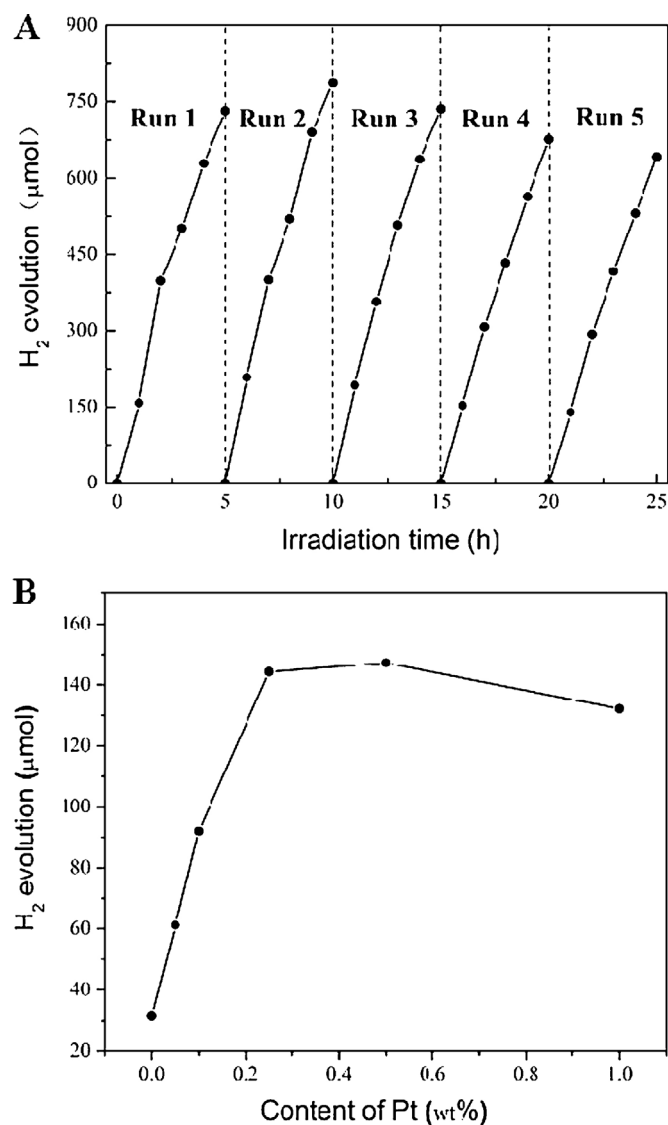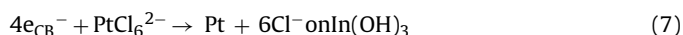

Fig. 6. A) Time courses of photocatalytic hydrogen evolution over ZIS-1.2 under visible light irradiation ($\lambda \geq 420$ nm). Conditions as in Fig. 5 except irradiation time. B) Effect of in-situ photodeposited Pt amount on the photocatalytic hydrogen evolution over ZIS-1.2 under visible light irradiation. Conditions as in Fig. 5 except Pt loading.

cess, the growth selectivity decreased, namely, ZIS-1.6 contained more H type heterojunctions (Fig. 3c) than ZIS-1.2 (Fig. 3a).

ZIS-1.2 can absorb visible light ($E_g = 2.46$ eV), whereas $In(OH)_3$ ($E_g = 5.17$ eV) cannot [48]. When J type $ZnIn_2S_4/In(OH)_3$ heterojunction is irradiated by visible light, the photoexcited electrons can transfer from the CB of $ZnIn_2S_4$ to that of $In(OH)_3$, which improves the charge separation. Fig. S7 gives plots of photocurrent against irradiation time. The photocurrent order is ZIS-1.2 > ZIS-1.6 > ZIS-TAA, in agreement with the activity order for the hydrogen evolution. This confirms also that the J type heterojunction can effectively separate the photogenerated carriers, whereas the H type one cannot.

For ZIS-1.2, the electrons transferred to $In(OH)_3$ can in-situ reduce $PtCl_6^{2-}$ into Pt.

$$ZnIn_2S_4 \xrightarrow{h\nu} e_{CB}^- + h_{VB}^+ \qquad (6)$$

$$4e_{CB}^- + PtCl_6^{2-} \rightarrow Pt + 6Cl^- \text{ on} In(OH)_3 \qquad (7)$$

TEM image (Fig.S8 a) shows that Pt particles are loaded on the rims of $ZnIn_2S_4$ nanosheets. HRTEM image indicates that Pt par-
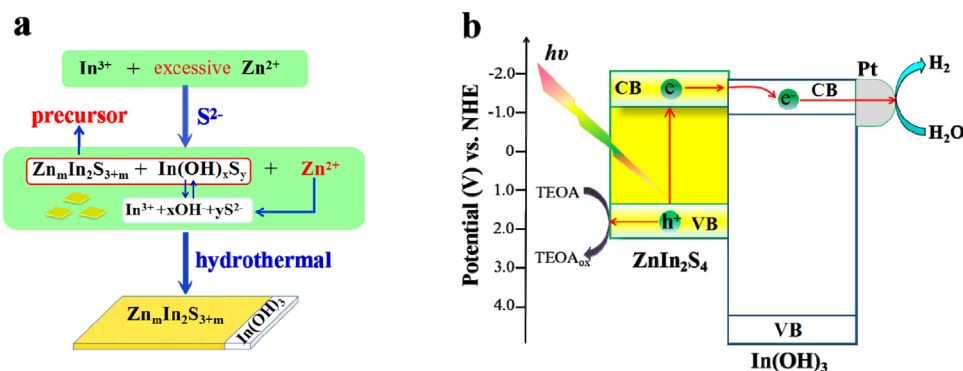
Scheme 2. a) Schematic formation of J type $Zn_mIn_2S_{3+m}/In(OH)_3$ heterojunction by the hydrothermal transformation, b) Proposed mechanism for photocatalytic hydrogen evolution over $ZnIn_2S_4/In(OH)_3$ heterojunction with in situ photodeposited Pt.

ticles are selectively loaded on the rim $In(OH)_3$ rather than on the $ZnIn_2S_4$ nanosheet plane (Fig.S8 b), which can be proved by the lattice fringe with interplanar spacing of 0.227 nm for (111) plane of face-centered cubic Pt [49]. The selective Pt loading supports further the formation of the J type heterojunction for ZIS-1.2 instead of the H type one. As shown in Fig. 6B, the optimal Pt-loading (0.25 wt%) for ZIS-1.2 is much lower than the reported values (1.0 and 3.0 wt%) for $ZnIn_2S_4$ [16,18]. This is because the content of the rim $In(OH)_3$ is significantly less than that of the sheet-like $ZnIn_2S_4$ (Figs. 3 and 4) and Pt is selectively loaded on $In(OH)_3$.

After the Pt deposition, the transferred electron can be trapped by the deposited Pt to reduce water into H_2.

$$H^+(H_2O) + {}^\bullet e_{CB}{}^- \rightarrow 1/2\,H_2\,onPt \tag{8}$$
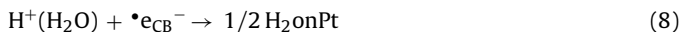
The photoexcited hole is scavenged by the electron donor TEOA.

$$h_{VB}{}^+ + TEOA \rightarrow EY + TEOA_{OX} \tag{9}$$

Based on the above discussion, the proposed mechanism for the enhanced photocatalytic H_2 evolution over ZIS-1.2 with Pt as a cocatalyst under visible light irradiation is described as Scheme 2b.

5. Conclusions

The new concept of anisotropic heterojunctions was created for layered semiconductors. Compared to the H type, the J type heterostructure exhibits efficient transfer and separation of the photoinduced carrier pairs. Furthermore, for ZIS-1.2, $ZnIn_2S_4/In(OH)_3$ heterojunction with J type structure was successfully fabricated by a simple hydrothermal transformation of the co-precipitation precursor in the presence of excessive Zn^{2+} ions. The heterojunction with in-situ photodeposited Pt shows efficient and stable photocatalytic H_2 evolution under visible irradiation, leading to a high AQY of 38.3% at 420 nm with a low optimal Pt loading of 0.25 wt%.

Acknowledgements

Appendix A. Supplementary data

Supplementary data associated with this article can be found, in the online version, at http://dx.doi.org/10.1016/j.apcatb.2017.01.062.

References

[1] X.B. Chen, S.H. Shen, L.J. Guo, S.S. Mao, Semiconductor-based photocatalytic hydrogen generation, Chem. Rev. 110 (2010) 6503–6570.

[2] Y.X. Li, H. Wang, S.Q. Peng, Tunable photodeposition of MoS_2 onto a composite of reduced graphene oxide and CdS for synergic photocatalytic hydrogen generation, J. Phys. Chem. C 118 (2014) 19842–19848.

[3] W.Y. Zhang, Y.X. Li, S.Q. Peng, Facile synthesis of graphene sponge from graphene oxide for efficient dye-sensitized H_2 evolution, ACS Appl. Mater. Interface 8 (2016) 15187–15195.

[4] Y. Ma, X.L. Wang, Y.S. Jia, X.B. Chen, H.X. Han, C. Li, Titanium dioxide-based nanomaterials for photocatalytic fuel generations, Chem. Rev. 114 (2014) 9987–10043.

[5] W.Y. Zhang, Y.X. Li, X.P. Zeng, S.Q. Peng, Synergetic effect of metal nickel and graphene as a cocatalyst for enhanced photocatalytic hydrogen evolution via dye sensitization, Sci. Rep. 5 (2015) 10589.

[6] J.Y. Xu, Y.X. Li, S.Q. Peng, G.X. Lu, S.B. Li, Eosin Y-sensitized graphitic carbon nitride fabricated by heating urea for visible light photocatalytic hydrogen evolution: the effect of the pyrolysis temperature of urea, Phys. Chem. Chem. Phys. 15 (2013) 7657–7665.

[7] K. Maeda, K. Domen, Photocatalytic water splitting: recent progress and future challenges, J. Phys. Chem. Lett. 1 (2010) 2655–2661.

[8] C.L. Li, Z.Q. Lei, Q.Z. Wang, F. Cao, F. Wang, W.F. Shangguan, Synthesis of $TiO_2(B)$ nanobelts photocatalyst for water splitting to H_2, J. Mol. Catal. 29 (2015) 382–389.

[9] I. Tsuji, H. Kato, H. Kobayashi, A. Kudo, Photocatalytic H_2 evolution reaction from aqueous solutions over band structure-controlled $(AgIn)_{(x)}Zn_{2(1-x)}S_2$ solid solution photocatalysts with visible-light response and their surface nanostructures, J. Am. Chem. Soc. 126 (2004) 13406–13413.

[10] J. Zhang, J.G. Yu, M. Jaroniec, J.R. Gong, Noble metal-free reduced graphene oxide-$Zn_xCd_{1-x}S$ nanocomposite with enhanced solar photocatalytic H_2-production performance, Nano Lett. 12 (2012) 4584–4589.

[11] Y.X. Li, D. Gao, S.Q. Peng, G.X. Lu, S.B. Li, Photocatalytic hydrogen evolution over $Pt/Cd_{0.5}Zn_{0.5}S$ from saltwater using glucose as electron donor: an investigation of the influence of electrolyte NaCl, Int. J. Hydrogen Energy 36 (2011) 4291–4297.

[12] S.Q. Peng, A. Ran, Y.X. Li, G.X. Lu, S.B. Li, Remarkable enhancement of photocatalytic hydrogen evolution over $Cd_{0.5}Zn_{0.5}S$ by bismuth-doping, Int. J. Hydrogen Energy 37 (2012) 1366–1374.

[13] X. Xu, R.J. Lu, X.F. Zhao, Y. Zhu, S.L. Xu, F.Z. Zhang, Novel mesoporous $Zn_xCd_{1-x}S$ nanoparticles as highly efficient photocatalysts, Appl. Catal. B: Environ. 125 (2012) 11–20.

[14] X. Xu, R.J. Lu, X.F. Zhao, S.L. Xu, X.D. Lei, F.Z. Zhang, D.G. Evans, Fabrication and photocatalytic performance of a $Zn_xCd_{1-x}S$ solid solution prepared by sulfuration of a single layered double hydroxide precursor, Appl. Catal. B: Environ. 102 (2011) 147–156.

[15] S.H. Shen, L. Zhao, L.J. Guo, Cetyltrimethylammoniumbromide (CTAB)-assisted hydrothermal synthesis of $ZnIn_2S_4$ as an efficient visible-light-driven photocatalyst for hydrogen production, Int. J. Hydrogen Energy 33 (2008) 4501–4510.

[16] B. Chai, T.Y. Peng, P. Zeng, X.H. Zhang, X.J. Liu, Template-free hydrothermal synthesis of $ZnIn_2S_4$ floriated microsphere as an efficient photocatalyst for H_2 production under visible-light irradiation, J. Phys. Chem. C 115 (2011) 6149–6155.

[17] Z. Lei, W. You, M. Liu, G. Zhou, T. Takata, M. Hara, K. Domen, C. Li, Photocatalytic water reduction under visible light on a novel $ZnIn_2S_4$ catalyst synthesized by hydrothermal method, Chem. Commun. (2003) 2142–2143.

[18] L. Shang, C. Zhou, T. Bian, H.J. Yu, L.-Z. Wu, C.-H. Tung, T.R. Zhang, Facile synthesis of hierarchical $ZnIn_2S_4$ submicrospheres composed of ultrathin mesoporous nanosheets as a highly efficient visible-light-driven photocatalyst for H_2 production, J. Mater. Chem. A 1 (2013) 4552–4558.

[19] Z.D. Xu, Y.X. Li, S.Q. Peng, G.X. Lu, S.B. Li, NaCl-assisted low temperature synthesis of layered Zn-In-S photocatalyst with high visible-light activity for hydrogen evolution, RSC Adv. 2 (2012) 3458–3466.
[20] S.Q. Peng, M. Ding, T. Yi, Y.X. Li, Photocatalytic hydrogen evolution in the presence of pollutant methylamines over Pt/ZnIn$_2$S$_4$ under visible light irradiation, J. Mol. Catal. 28 (2014) 466–473.
[21] G.P. Chen, N. Ding, F. Li, Y.Z. Fan, Y.H. Luo, D.M. Li, Q.B. Meng, Enhancement of photocatalytic H$_2$ evolution on ZnIn$_2$S$_4$ loaded with in-situ photo-deposited MoS$_2$ under visible light irradiation, Appl. Catal. B: Environ. 160–161 (2014) 614–620.
[22] S.H. Shen, L. Zhao, L.J. Guo, Zn$_m$In$_2$S$_{3+m}$ (m = 1–5, integer): A new series of visible-light-driven photocatalysts for splitting water to hydrogen, Int. J. Hydrogen Energy 35 (2010) 10148–10154.
[23] Z.W. Mei, S.X. Ouyang, D.-M. Tang, T. Kako, D. Golbergc, J.H. Ye, An ion-exchange route for the synthesis of hierachical In$_2$S$_3$/ZnIn$_2$S$_4$ bulk composite and its photocatalytic activity under visible-light irradiation, Dalton Trans. 42 (2013) 2687–2690.
[24] Q. Liu, H. Lu, Z.W. Shi, F.L. Wu, J. Guo, K.M. Deng, L. Li, 2D ZnIn$_2$S$_4$ nanosheet/1D TiO$_2$ nanorod heterostructure arrays for improved photoelectrochemical water splitting, ACS Appl. Mater. Interfaces 6 (2014) 17200–17207.
[25] Y.X. Li, J.X. Wang, S.Q. Peng, G.X. Lu, S.B. Li, Photocatalytic hydrogen generation in the presence of glucose over ZnS-Coated ZnIn$_2$S$_4$ under visible light irradiation, Int. J. Hydrogen Energy 35 (2010) 7116–7126.
[26] Y.J. Chen, G.H. Tian, Z.Y. Ren, K. Pan, Y.H. Shi, J.Q. Wang, H.G. Fu, Hierarchical core-shell carbon nanofiber@ZnIn$_2$S$_4$ composites for enhanced hydrogen evolution performance, Appl. Mater. Interfaces 6 (2014) 13841–13849.
[27] Y.J. Chen, H. Ge, L. Wei, Z.H. Li, R.S. Yuan, P. Liu, X.Z. Fu, Reduction degree of reduced graphene oxide (RGO) dependence of photocatalytic hydrogen evolution performance over rGO/ZnIn$_2$S$_4$ nanocomposites, Catal. Sci. Technol. 3 (2013) 1712–1717.
[28] L. Ye, J.L. Fu, Z. Xu, R.S. Yuan, Z.H. Li, Facile one-pot solvothermal method to synthesize sheet-on-sheet reduced graphene oxide (RGO)/ZnIn$_2$S$_4$ nanocomposites with superior photocatalytic performance, Appl. Mater. Interfaces 6 (2014) 3483–3490.
[29] L. Ye, Z.H. Li, Rapid microwave-assisted syntheses of reduced graphene oxide (RGO)/ZnIn$_2$S$_4$ microspheres as superior noble-metal-free photocatalyst for hydrogen evolutions under visible light, Appl. Catal. B: Environ. 160–161 (2014) 552–557.
[30] J.Y. Chen, H.M. Zhang, P.R. Liu, Y.B. Li, X.L. Liu, G.Y. Li, P.K. Wong, T.C. An, H.J. Zhao, Cross-linked ZnIn$_2$S$_4$/rGO composite photocatalyst for sunlight-driven photocatalytic degradation of 4-nitrophenol, Appl. Catal. B: Environ. 168–169 (2015) 266–273.
[31] Y.-J. Yuan, J.-R. Tu, Z.-J. Ye, D.-Q. Chen, B. Hu, Y.-W. Huang, T.-T. Chen, D.-P. Cao, Z.-T. Yu, Z.-G. Zou, MoS$_2$ -graphene/ZnIn$_2$S$_4$ hierarchical microarchitectures with an electron transport bridge between light-harvesting semiconductor and cocatalyst: a highly efficient photocatalyst for solar hydrogen generation, Appl. Catal. B: Environ. 188 (2016) 13–22.
[32] Z.Y. Zhang, K.C. Liu, A.Q. Feng, Y.N. Bao, B. Dong, Hierarchical sheet-on-Sheet ZnIn$_2$S$_4$/g-C$_3$N$_4$ heterostructure with highly efficient photocatalytic H$_2$ production based on photoinduced interfacial charge transfer, Sci. Rep. 6 (2016) 19221.

[33] L.K. Gallos, A.N. Anagnostopoulos, P. Argyrakis, Conduction anisotropy in layered semiconductors, Phys. Rev. B 50 (1994) 14643–14646.
[34] A.V. Anagnostopoulos, C. Manolikas, D. Papadopoulos, J. Spyridel, Composition faults in ZnIn$_2$S$_4$ (III) layered crystals and their influence on the anisotropic conductivity of this compound, Phys. Status Solidi A 72 (1982) 731–736.
[35] T.J. Yan, J.L. Long, X.C. Shi, D.H. Wang, Z.H. Li, X.X. Wang, Efficient photocatalytic degradation of volatile organic compounds by porous indium hydroxide nanocrystals, Environ. Sci. Technol. 44 (2010) 1380–1385.
[36] T.J. Yan, X.X. Wang, J.L. Long, P. Liu, X.L. Fu, G.Y. Zhang, X.Z. Fu, Urea-based hydrothermal growth, optical and photocatalytic properties of single-crystalline In(OH)$_3$ nanocubes, J. Colloid Interface Sci. 325 (2008) 425–431.
[37] T.J. Yan, J.L. Long, Y.S. Chen, X.X. Wang, D.Z. Li, X.Z. Fu, Indium hydroxide: a highly active and low deactivated catalyst for photoinduced oxidation of benzene, C. R. Chimie 11 (2008) 101–106.
[38] T.J. Yan, X.X. Wang, J.L. Long, H.X. Lin, R.S. Yuan, W.X. Dai, Z.H. Li, X.Z. Fu, Controlled preparation of In$_2$O$_3$, InOOH and In(OH)$_3$ via a one-pot aqueous solvothermal route, New J. Chem. 32 (2008) 1843–1846.
[39] J.J. Guo, S.X. Ouyang, T. Kako, J.H. Ye, Mesoporous In(OH)$_3$ for photoreduction of CO$_2$ into renewable hydrocarbon fuels, Appl. Surf. Sci. 280 (2013) 418–423.
[40] W.W. He, H.M. Jia, D.F. Yang, P. Xiao, X.L. Fan, Z. Zheng, H.-Y. Kim, W.G. Wamer, J.-J. Yin, Composition directed generation of reactive oxygen species in irradiated mixed metal sulfides correlated with their photocatalytic activities, ACS Appl. Mater. Interface 7 (2015) 16440–16449.
[41] L.Z. Wan, T. Sasaki, Titanium oxide nanosheets: graphene analogues with versatile functionalities, Chem. Rev. 114 (2014) 9455–9486.
[42] C.N.R. Rao, K. Gopalakrishnan, U. Maitra, Comparative study of potential applications of graphene MoS$_2$, and other two-dimensional materials in energy devices, sensors, and related areas, ACS Appl. Mater. Interfaces 7 (2015) 7809–7832.
[43] S.W. Cao, J.G. Yu, g-C$_3$N$_4$-based photocatalysts for hydrogen generation, J. Phys. Chem. Lett. 5 (2014) 2101–2107.
[44] C.W. Tana, G.Q. Zhua, M. Hojamberdiev, K.S. Lokesh, X.C. Luo, L. Jin, J.P. Zhou, P. Liu, Adsorption and enhanced photocatalytic activity of the {0 0 0 1} faceted Sm-doped ZnIn$_2$S$_4$ microspheres, J. Hazard. Mater. 278 (2014) 572–583.
[45] G. Biedermann, N.C. Li, J. Yu, Studies on the hydrolysis of metal ions: part 34. The hydrolysis of the indium(III) ion, In^{3+}, in 3 M (Na$^+$) Cl$^-$ medium, Acta Chem. Scand. 15 (1961) 555–564.
[46] M.J. Barnabas, S. Parambadath, A. Mathew, S.S. Park, A. Vinu, C.-S. Ha, Highly efficient and selective adsorption of In^{3+} on pristine Zn/Al layered double hydroxide (Zn/Al-LDH) from aqueous solutions, J. Solid State Chem. 233 (2016) 133–142.
[47] R. Bayon1, R. Musembi, A. Belaidi, M. Bär, T. Guminskaya, M.-Ch. Lux-Steiner, Th. Dittrich, Highly structured TiO$_2$/In(OH)$_x$S$_y$/PbS/PEDOT:PSS for photovoltaic applications, Sol. Energy Mater. Sol. Cells 89 (2005) 13–25.
[48] Z.B. Lei, G.J. Ma, M.Y. Liu, W.S. You, H.J. Yan, G.P. Wu, T. Takata, M. Hara, K. Domen, C. Li, Sulfur-substituted and zinc-doped In(OH)$_3$: a new class of catalyst for photocatalytic H$_2$ production from water under visible light illumination, J. Catal. 237 (2006) 322–329.
[49] W.Y. Zhang, Y.X. Li, S.Q. Peng, X. Cai, Enhancement of photocatalytic H$_2$ evolution of eosin Y-sensitized reduced graphene oxide by a simple photoreaction, Beilstein J. Nanotechnol. 5 (2014) 801–811.